nanomaterials

MDPI

Article

Macromolecules with Different Charges, Lengths, and Coordination Groups for the Coprecipitation Synthesis of Magnetic Iron Oxide Nanoparticles as T_1 MRI Contrast Agents

Cheng Tao †, Yanan Chen †, Danli Wang, Yu Cai, Qiang Zheng, Lu An, Jiaomin Lin *, Qiwei Tian and Shiping Yang *

The Key Laboratory of Resource Chemistry of the Ministry of Education, The Shanghai Key Laboratory of Rare Earth Functional Materials, and The Shanghai Municipal Education Committee Key Laboratory of Molecular Imaging Probes and Sensors, Shanghai Normal University, Shanghai 200234, China; 1000441586@smail.shnu.edu.cn (C.T.); 1000441335@smail.shnu.edu.cn (Y.C.); wdl2011520@163.com (D.W.); 1000442867@smail.shnu.edu.cn (Y.C.); diwuxiaoo@163.com (Q.Z.); anlu1987@shnu.edu.cn (L.A.); qiweitian@shnu.edu.cn (Q.T.)

* Correspondence: linjm@shnu.edu.cn (J.L.); shipingy@shnu.edu.cn (S.Y.)

† These authors contributed equally to this work.

Received: 15 March 2019; Accepted: 19 April 2019; Published: 5 May 2019

Abstract: Considerable efforts have been focused on the exploitation of macromolecule ligands for synthesis of magnetic Fe_3O_4 nanoparticles as T_1 magnetic resonance imaging (MRI) contrast agents, but studies that concern macromolecule ligands with different charges and coordination groups are still limited. Herein, we used poly(acrylic acid) (PAA), poly(allylamine hydrochloride) (PAH), and polyvinyl alcohol (PVA), which possess negative, positive and neutral charges with carboxylic acid, amino and hydroxyl groups respectively, as templates and stabilizers to fabricate Fe_3O_4 nanoparticles through coprecipitation reaction. The obtained Fe_3O_4-PAA, Fe_3O_4-PAH, and Fe_3O_4-PVA nanoparticles showed T_1 contrast performance with r_1 relaxivities of 23.4, 60.3, and 30.6 mM s^{-1} at 0.5 T (25 °C), and a r_2/r_1 ratio of 2.62, 3.82, and 7.26, respectively. The cell viability assay revealed that Fe_3O_4-PAA and Fe_3O_4-PVA exhibited good biocompatibility, while Fe_3O_4-PAH displayed high cytotoxicity. In vivo T_1-weighted (1 T) mice showed that both Fe_3O_4-PAA and Fe_3O_4-PVA were able to display remarkably brighten the contrast enhancement for the mice tumor and kidney sites, but Fe_3O_4-PAA had better contrast performance. This work highlights that the macromolecule ligands play an important role in the biocompatibility and T_1 contrast performance of magnetic Fe_3O_4 nanoparticles.

Keywords: T_1-weight contrasts; iron oxide; surface charge; coprecipitation synthesis; MRI

1. Introduction

In the past decade, the utilization of magnetic iron oxide (Fe_3O_4) nanoparticles as a T_1-weighted contrast for magnetic resonance imaging (MRI) has received tremendous attention [1–6]. On the one hand, Fe_3O_4 nanoparticles have better biocompatibility compared to currently widely-used clinical Gd-chelate T_1 contrast agents, such as Gd-DTPA and Gd-DTOA [7–12]. The Gd-chelates have great potential accumulative toxicity (e.g., nephrogenic systemic fibrosis) caused by the leaching out of the Gd ions from the chelate ligand [13], while the Fe_3O_4 nanoparticles can be degraded in the body and the released iron ions can be subsequently incorporated into iron pools and metabolic processes [10]. On the other hand, Fe_3O_4 nanoparticles with a small size and suitable surface state are

able to display a high longitudinal relaxation rate (r_1) [14–18], which can significantly improve the spatial resolution of the T_1-weighted image for some special sites such as blood vessels and vascular organs. Nevertheless, small Fe_3O_4 nanoparticles without appropriate ligands decorated on the surface tend to form aggregation and subsequently display T_2 rather than T_1 contrast enhancement [19,20].

To improve the T_1 contrast performance and prevent the aggregation of nanoparticles in vivo, great efforts have recently been focused on the synthesis and surface modification of Fe_3O_4 nanoparticles [21–25]. The coprecipitation reaction of Fe^{2+} and Fe^{3+} ions under alkaline conditions is a traditional and widely-used method to fabricate Fe_3O_4 nanoparticles [26–30]. Compared with some other methods, such as thermal decomposition [31–33] and hydrothermal and solvothermal methods [34–37], coprecipitation is more convenient since it can be carried out in water phase without the further requirement of surfactant modification to improve the water-dispersibility of the obtained nanoparticles. Besides, similar to the approach of microwave-assisted synthesis [6,38], the coprecipitation method is a procedure that can be easily scaled up [39]. However, because the reaction is carried out in water phase and the reaction speed is very fast for coprecipitation, controlling the size and preventing the aggregation of the produced Fe_3O_4 nanoparticles are always important and challenging issues [40]. Using functional macromolecule ligands as templates and stabilizers has proved to be an effective approach to overcome these challenges [37,39–42]. The affinity coordination groups, such as the hydroxyl and carboxylic acid groups from the macromolecule ligands, can coordinate with the iron ions and thus control the growth of the nanoparticle seed and prevent the aggregation of the produced nanoparticles [43]. For example, Rui et al. used poly(acrylic acid) to synthesize Fe_3O_4 nanoparticles with a small size and high relaxivity for in vivo T_1-weighted imaging [39]. Li et al. developed poly(acrylic acid)-poly(methacrylic acid) for the synthesis of small Fe_3O_4 nanoparticles with good water-dispersibility and remarkable T_1 contrast performance [26].

To date, a great number of macromolecule ligands have been utilized as templates and stabilizers to fabricate hydrophilic small Fe_3O_4 nanoparticles as T_1 contrast agents [26,27,44–46], but studies that concern the use of different charges and coordination groups of macromolecule ligands are still limited [47,48]. Indeed, the charges of macromolecule ligands are also an important parameter for controlling the size and preventing the aggregation of the Fe_3O_4 nanoparticles, since they usually correspond to the coordination affinity between the coordination groups and metal ions, and the electrostatic interaction between adjacent nanoparticles. In this work, we used three macromolecule ligands that possessed negative, positive and neutral charges with carboxylic acid, amino and hydroxyl groups, respectively, as templates and stabilizers for the coprecipitation synthesis of small magnetic Fe_3O_4 nanoparticles (Scheme 1), which showed differences in size, water-dispersibility, cytotoxicity and T_1-weight contrast performance.

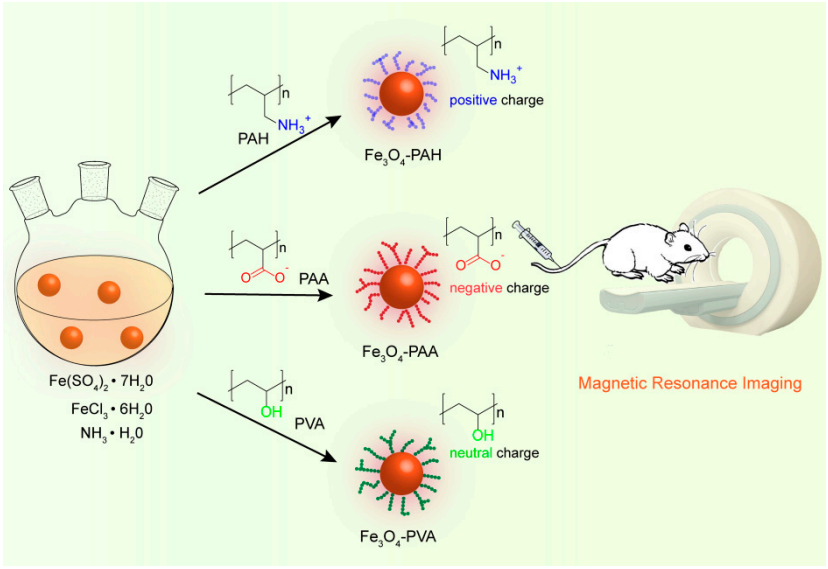

Scheme 1. Schematic illustration of the coprecipitation synthesis of Fe_3O_4-poly(acrylic acid) (PAA), Fe_3O_4-poly(allylamine hydrochloride) (PAH), and Fe_3O_4-polyvinyl alcohol (PVA) with negative, positive and neutral charges, respectively, as the T_1-weight contrast agent.

2. Materials and Methods

2.1. Materials

$Fe(SO_4)_2 \cdot 7H_2O$, $FeCl_3 \cdot 6H_2O$ and NH_3 solution (25%) were obtained from Sigma Aldrich (Saint Louis, MO, USA). Poly(allylamine hydrochloride) (PAH, average Mw ~ 17,500), poly(acrylic acid) (PAA, average Mw ~ 2000) and polyvinyl alcohol (PVA, average Mw ~ 20,000–30,000) were purchased from Alfa (Heysham, UK). All chemicals were used without further purification.

2.2. Synthesis of Fe_3O_4-PAH, Fe_3O_4-PAA and Fe_3O_4-PVA Nanoparticles

The synthetic procedures for Fe_3O_4-PAH, Fe_3O_4-PAA and Fe_3O_4-PVA nanoparticles were quite similar, excepting the use of different polymer ligands as templates and stabilizers. Typically, the polymer ligand (140 mg) was added to a 250 mL three-necked flask with 50 mL of deionized water, and then stirred for 1 h under N_2 atmosphere to remove the oxygen in the flask. Then 0.25 mmol of $Fe(SO_4)_2 \cdot 7H_2O$ (70 mg) and 0.52 mmol of $FeCl_3 \cdot 6H_2O$ (140 mg) were dissolved in 2 mL of deionized water, and injected into the three-necked flask. The above mixture was slowly heated to 90 °C, and then 5 mL of concentrated ammonia solution was rapidly injected under vigorous stirring. The reaction was kept at 90 °C for a further 2 h and then cooled down to room temperature. The black suspension was ultrafiltration centrifugation (with 10-k ultra-filtration centrifuge tube) and was washed with deionized water 3–4 times.

2.3. Characterization

The structure of the obtained Fe_3O_4 nanoparticles was determined by Powder X-ray diffractometer (PXRD, Bruker, D8 ADVANCE, Cu K-α, Brucker, Karlsruhe, Germany). To verify the macromolecule ligand coating, Fourier-transform IR spectra (Nicolet Avatar 370 FT-IR, Thermo Electron Corporation, Madison, WI, USA) with potassium bromide as pressed pellets was carried out on a Nicolet Avatar 370 FT-IR spectrophotometer. The hydrodynamic size and zeta potential studies were carried out on a Malvern Zetasizer Nano ZS (Malvern, UK, scattering angle, 90°; temperature, 25 °C; refraction indexes of H_2O and Fe_3O_4, 1.33 and 2.30, respectively). The morphology and size were evaluated using transmission electron microscopy (JEOL JEM-2010 microscopy, JEOL, Tokyo, Japan). The magnetic

properties were measured using a superconducting quantum interference device (Lake Shore (Carson, CA, USA)). The concentration of nanoparticles was determined by dissolution in concentrated nitric acid (15 mol/L) and then ironion concentration was measured using high-dispersion inductively coupled plasma atomic emission spectroscopy (Teledyne Leeman Labs, Prodigy, Inc., Hudson, NH, USA). The longitudinal and transverse relaxation times (T_1 and T_2, respectively) for calculating the relaxation rate (r_1 and r_2, respectively) were measured on a magnetic resonance scanner (0.5 T, NMI20, Niumag, Shanghai, China) with parameters of DRG1, 3; TW, 8000 ms; RG, 20 db; SW, 100 kHz; SF, 18 MHz. T_1-weighted images were obtained with the parameters of TR, 300 ms; TE, 0.04 ms; and T_2-weighted images were acquired with parameters of TR, 4500 ms; TE, 100 ms.

2.4. In Vitro Cytotoxicity Assay

The cytotoxicity of Fe_3O_4-PAA, Fe_3O_4-PAH, and Fe_3O_4-PVA nanoparticles were evaluated using standard methyl thiazolyltetrazolium (MTT) assay with 4T1 cell lines (a mouse breast cancer cell line). The 4T1 cells were purchased from Shanghai Institutes for Biological Sciences. The MTT assay was carried out according to the following procedures. 4T1 cells (5×10^4 cells/well) were first plated in a 96-well plate for 24 h and then treated with different concentrations (0, 5, 12.5, 25, 50, and 100 μg/mL) of Fe_3O_4-PAA, Fe_3O_4-PAH, or Fe_3O_4-PVA nanoparticles in dulbecco's modified eagle medium (DMEM) for 12 or 24 h at 37 °C with 5% CO_2. After that the medium was removed and the cells were washed with phosphate buffered saline (PBS), and then 20 μL (5 mg/mL) of thiazolyl blue tetrazolium bromide was added and the cells were incubated for a further 4 h. The medium was carefully removed and the remaining purple formazan crystals were lysed with 150 μL of dimethyl sulfoxide. The absorption of the formazan at 490 nm for calculating the cell viability was measured using a Multiskan MK3 microplate reader (Thermo Fisher Scientific, Waltham, MA, USA).

2.5. In Vivo Magnetic Resonance Imaging

To evaluate in vivo the MRI properties of Fe_3O_4-PAA and Fe_3O_4-PVA, T_1-weighted images of mice bearing 4T1 tumor were carried out on a 1.0 T MRI scanner (NM42-040H-I; Niumag, Shanghai, China). The intravenous injecting dose of materials was 1.3 mg Fe/kg body weight. During imaging, the mice were anesthetized with 8% chloral hydrate. The T_1-weighted imaging parameters were the following: field of view, 100 × 100 mm; slice thickness, 3 mm; echo time, 20 ms; repetition time (TR), 300 ms; matrix size, 256 × 192 mm. The operations of all animal methods were carried out strictly according to the requirements of the Animal Ethics Committee of the Shanghai Normal University (approval code No: 2018-0127).

3. Results and Discussion

3.1. Synthesis and Characterization

Giving that poly(acrylic acid) (PAA), poly(allylamine hydrochloride) (PAH), and polyvinyl alcohol (PVA) possess negative, positive and neutral charges with carboxylic acid, amino and hydroxyl coordination groups respectively, we used them as templates and stabilizers to fabricate Fe_3O_4 nanoparticles (denoted as Fe_3O_4-PAA, Fe_3O_4-PAH, and Fe_3O_4-PVA, respectively) through the coprecipitation reaction [49]. Typically, $FeCl_3$, $Fe(SO_4)_2$ and PAA/PAH/PVA were mixed in deionized water and heated to 90 °C under a nitrogen atmosphere. Concentrated ammonia solution (25%) that served as the alkali was injected into the mixture to trigger the formation of Fe_3O_4 nanoparticles. In the beginning, the aqueous solution of iron ions and PAA, PAH or PVA were tawny and opaque. The pH of PAA, PAH and PVA in aqueous solution was 2.9, 5.8 and 3.8, respectively, and upon addition of ferric/ferrous salt, the corresponding pH changed to 1.5, 2.2 and 2.0, respectively. After the addition of concentrated ammonia solution, the reaction mixture became black immediately, suggested the formation of Fe_3O_4 nanoparticles.

Transmission electron microscopy (TEM) images showed that the average diameters of Fe_3O_4-PAA, Fe_3O_4-PAH, and Fe_3O_4-PVA nanoparticles were 4.5 ± 0.8 and 7.4 ± 1.3 and 2.8 ± 0.4 nm, respectively (Figure S1). The slightly different sizes of the nanoparticles indicated the different capabilities of PAA, PAH and PVA as templates and stabilizers in controlling the growth of the Fe_3O_4 seeds. The crystalline structures and phase composition of the as-synthesized nanoparticles were characterized via X-ray diffraction (XRD). As shown in Figure 1d, Fe_3O_4-PAA, Fe_3O_4-PAH, and Fe_3O_4-PVA have similar diffraction peaks, suggesting that they are all crystalline, which is important for magnetic nanoparticles. The 2-theta peaks at 30.4, 35.8, 43.5, 53.9, 57.5 and 63.2° were able to be indexed to {311}, {222}, {400}, {422}, {511} and {440} lattice planes of the cubic phase Fe_3O_4 (JCPDS No. 75-1449). No other peaks that belonged to this phase were observed for the three samples, confirming the successful fabrication of the pure phase Fe_3O_4. Fe_3O_4-PAA, Fe_3O_4-PAH, and Fe_3O_4-PVA exhibited good solubility in the aqueous solution (Figure 1e). The hydrodynamic size of Fe_3O_4-PAA, Fe_3O_4-PAH, and Fe_3O_4-PVA determined by dynamic light scattering (DLS) were around 56, 229 and 141 nm, respectively (Figure S2). Compared to the size observed from the TEM images, the larger hydrodynamic size of Fe_3O_4-PAA can be attributed to the surrounding macromolecule ligands and water molecules on the surface of the nanoparticles. Nevertheless, the hydrodynamic size of Fe_3O_4-PAH and Fe_3O_4-PVA were obviously larger than that observed in TEM images, suggesting the slight aggregation of Fe_3O_4-PAH and Fe_3O_4-PVA in the aqueous solution. The zeta potential of Fe_3O_4-PAA, Fe_3O_4-PAH, and Fe_3O_4-PVA was determined to be −35.8, 39.0, and −1.1 mV, respectively (Figure 2b). The negative, positive and nearly neutral zeta potential of Fe_3O_4-PAA, Fe_3O_4-PAH, and Fe_3O_4-PVA were consistent with that of the PAA, PAH and PVA (−19.2, 25, and −0.83 mV, respectively), indicating the existence of macromolecule ligands on the surface of the nanoparticles.

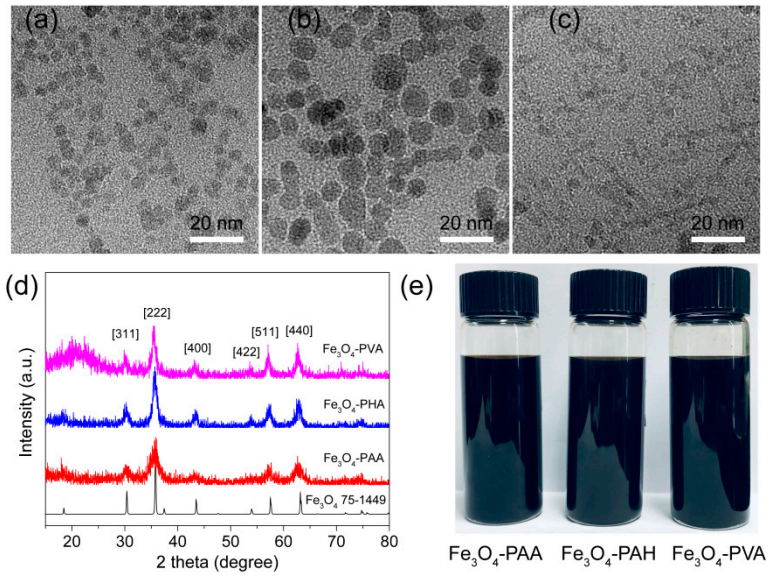

Figure 1. TEM images of (**a**) Fe_3O_4-PAA, (**b**) Fe_3O_4-PAH, and (**c**) Fe_3O_4-PVA. (**d**) PXRD of the Fe_3O_4 powder standard with JCPDS Card No. of 75-1449, Fe_3O_4-PAA, $Fe_{3+}O_4$-PAH and Fe_3O_4-PVA. (**e**) Photographs of Fe_3O_4-PAA, Fe_3O_4-PAH and Fe_3O_4-PVA nanoparticles in aqueous suspension.

The surface functionalization of the Fe_3O_4 nanoparticles with PAA, PAH and PVA ligands was further confirmed by Fourier transform infrared (FT-IR) spectrum. As shown in Figure 2a, Fe_3O_4-PAA, Fe_3O_4-PAH, and Fe_3O_4-PVA exhibited a characteristic absorption peak of around 564–610 cm^{-1}, which arose from the vibration band of Fe–O, suggesting the formation of Fe_3O_4. For PAA and Fe_3O_4-PAA, the absorption bands around 3200–3600 cm^{-1} can be attributed to the O–H stretching vibrations. The characteristic absorption peaks at 1712 and 1401 cm^{-1} were due to the C=O stretching vibrations and C–O stretching vibrations of carboxylic acid groups in the PAA, respectively [39]. The characteristic

absorption bands for PAH and Fe_3O_4-PAH were observed at 3402, 3023 and 1604 cm^{-1}, and can be attributed to the N–H stretching and bending vibrations, respectively. The absorption peak at 1113 cm^{-1} was due to the C–N stretching vibration [50]. For PVA and Fe_3O_4-PVA, characteristic absorption peaks were observed around 3200–3600 cm^{-1} (O–H stretching vibrations), 2940 cm^{-1} (–CH_2– symmetric vibrations), 1094 and 1438 cm^{-1} (C–O stretching vibrations) [51]. The characteristic absorption of PAA, PAH and PVA can be observed in that of Fe_3O_4-PAA, Fe_3O_4-PAH, and Fe_3O_4-PVA, respectively, demonstrating the presence of macromolecules with the nanoparticles.

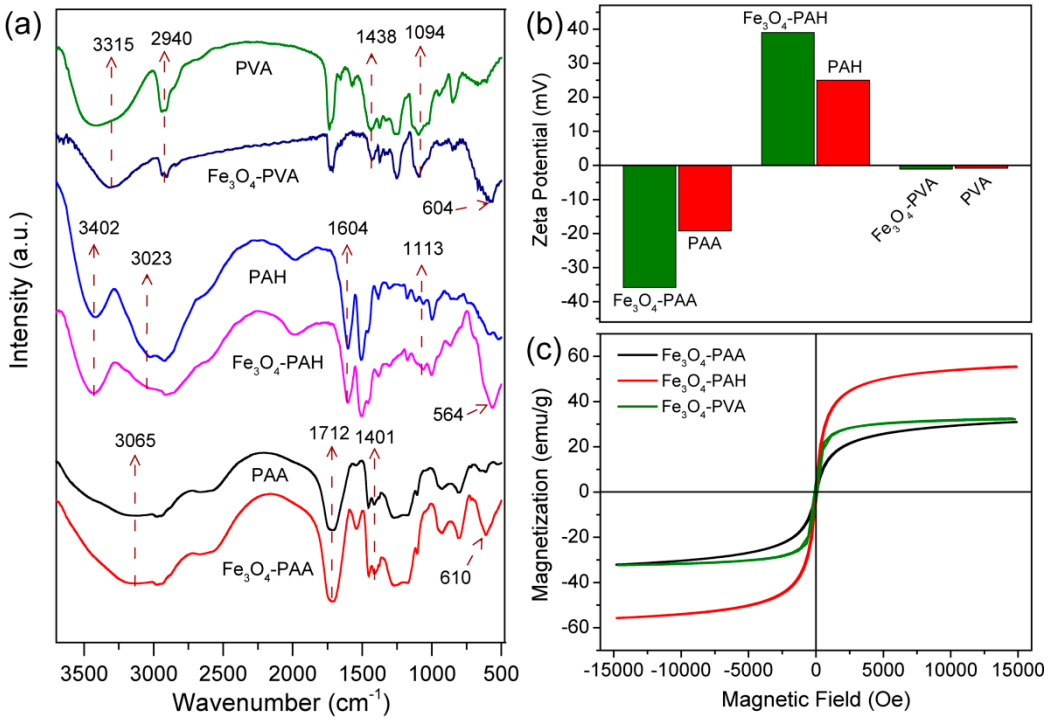

Figure 2. (**a**) FTIR spectroscopy and (**b**) Zeta potential of Fe_3O_4-PAA, PAA, Fe_3O_4-PAH, PAH, Fe_3O_4-PVA and PVA. (**c**) Field-dependent magnetization curves for Fe_3O_4-PAA, Fe_3O_4-PAH, and Fe_3O_4-PVA nanoparticles at 298 K.

To evaluate whether the obtained Fe_3O_4 nanoparticles were superparamagnetic, which is crucial for magnetic Fe_3O_4 to be used as a T_1-weighted MRI contrast agent, the magnetization curves for Fe_3O_4-PAA, Fe_3O_4-PAH, and Fe_3O_4-PVA with a magnetic field up to 1.5 T were measured at 298 K. The saturation magnetization for Fe_3O_4-PAA, Fe_3O_4-PAH, and Fe_3O_4-PVA were determined to be 32.1, 55.2 and 32.5 emu/g, respectively (Figure 2c). The inductively coupled plasma-atomic emission spectrometry (ICP-AES) results revealed that the ratios of Fe_3O_4 to the total weight were 70.1% for Fe_3O_4-PAA, 73.6% for Fe_3O_4-PAH, and 44.6% for Fe_3O_4-PVA. Compared with Fe_3O_4-PAH, the Fe_3O_4-PAA and Fe_3O_4-PVA with smaller diameters exhibited lower saturation magnetization, which can be ascribed to the higher specific surface associated with spin-canting [52]. According to the hysteresis loops, the coercivity and remanence for Fe_3O_4-PAA, Fe_3O_4-PAH, and Fe_3O_4-PVA were all negligible at room temperature, indicating their superparamagnetic behavior.

3.2. Magnetic Resonance Imaging

To assess the MRI properties of Fe_3O_4-PAA, Fe_3O_4-PAH, and Fe_3O_4-PVA, the T_1-weighted image and longitudinal and transverse relaxation time (T_1 and T_2, respectively) with different concentrations of materials in aqueous solution at 25 °C were studied using a 0.5 T MRI scanner. As shown in Figure 3d, with the increasing concentration of materials, all the T_1-weighted images of Fe_3O_4-PAA, Fe_3O_4-PAH, and Fe_3O_4-PVA gradually brightened, indicating that they were able to exhibit T_1-weighted

contrast [45]. According to the slope of the relaxometric curves (Figure 3a–c), the longitudinal molar relaxivities (r_1) for Fe_3O_4-PAA, Fe_3O_4-PAH, and Fe_3O_4-PVA were calculated to be 23.6, 60.8, and 30.9 mM s^{-1}, respectively, which are relatively high values as compared to some reported relaxivities for Fe_3O_4 nanoparticles using similar synthesis methods [53]. The high r_1 relaxivity of these nanoparticles should be attributed to their small size and high surface decorated with hydrophilic macromolecules, which can facilitate the water exchange rate between the surrounding bulk water molecules, and which coordinated with the Fe ions. The transverse molar relaxivities (r_2) for Fe_3O_4-PAA, Fe_3O_4-PAH, and Fe_3O_4-PVA were determined to be 62.3, 232.3 and 224.5 mM s^{-1}, respectively. Generally, the r_2/r_1 ratio is a crucial parameter for assessing the T_1 performance of contrast agents. The r_2/r_1 ratio for Fe_3O_4-PAA, Fe_3O_4-PAH, and Fe_3O_4-PVA was calculated to be 2.64, 3.82 and 7.27, respectively. For Fe_3O_4-PAA, the low r_2 and r_2/r_1 ratio indicated that it is adequate as a T_1-weighted contrast agent.

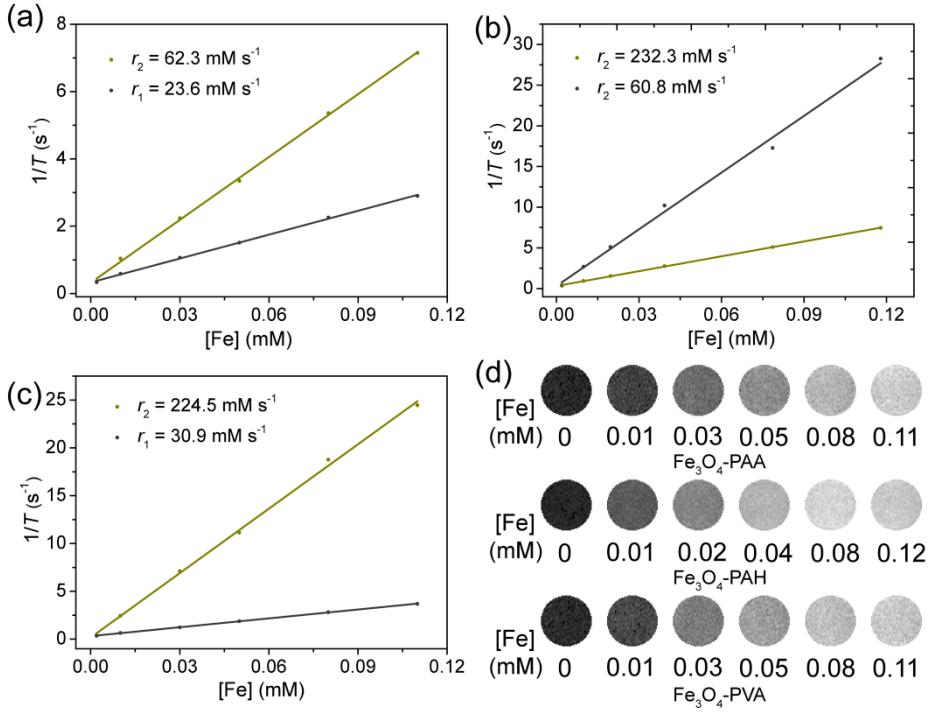

Figure 3. Plot of 1/*T* against Fe concentration for (**a**) Fe_3O_4-PAA, (**b**) Fe_3O_4-PAH, and (**c**) Fe_3O_4-PVA nanoparticles. The values of $r_1$and r_2 were calculated based on the slopes of the corresponding fitting lines (B_0 = 1 T, 25 °C). The T_1° and T_2° values of pure water were 2.79 and 3.01 s, respectively. (**d**) T_1-weight MR images of the aqueous dispersion of Fe_3O_4-PAA, Fe_3O_4-PAH, and Fe_3O_4-PVA nanoparticles with different Fe concentrations.

3.3. In Vitro Cytotoxicity

Encouraged by the good T_1 contrast performance of Fe_3O_4-PAA, Fe_3O_4-PAH, and Fe_3O_4-PVA, their biocompatibility was assessed before in vivo tests. The cytotoxicity of Fe_3O_4-PAA, Fe_3O_4-PAH, and Fe_3O_4-PVA were investigated using 4T1 cell lines with standard methyl thiazolyltetrazolium (MTT) assay. For Fe_3O_4-PAA and Fe_3O_4-PVA, no significant cytotoxicity was observed after incubation with a different concentration of nanoparticles (0–100 μg mL^{-1} based on Fe) for 12 and 24 h. For Fe_3O_4-PAH, a significant decrease in the cell viability was observed even with very low concentrations of material. As shown in Figure 4a,c, the 4T1 cell that incubated with Fe_3O_4-PAA and Fe_3O_4-PVA remained viable above 94% and 84%, respectively, when the concentration of Fe ions was up to 100 μg mL^{-1} and the incubation time was prolonged to 24 h, indicating lower cytotoxicity for Fe_3O_4-PAA and Fe_3O_4-PVA within the investigated concentration. Nevertheless, the cells that were incubated with Fe_3O_4-PAH had a viability of only about 8%, although the concentration of Fe ions was only 25 μg mL^{-1} and the

incubation time was only 12 h, suggesting a very large cytotoxicity of Fe_3O_4-PAH (Figure 4b). Generally, the cytotoxicity of a nanomaterial is associated with the surface properties of the nanoparticles. For Fe_3O_4-PAA, the low cytotoxicity of our results was in agreement with those reported in the literature, which showed that PAA-coated magnetic nanoparticles with highly negative zeta potential have good biocompatibility and are not internalized by biological cells [54]. For Fe_3O_4-PAH, the large cytotoxicity may be attributed to the abundant amino groups that have a high pKa value (around 9) of the PAH ligand on the surface of the Fe_3O_4 nanoparticles [48]. Due to the large cytotoxicity of Fe_3O_4-PAH, only Fe_3O_4-PAA and Fe_3O_4-PVA were used for further in vivo T_1 MRI investigation.

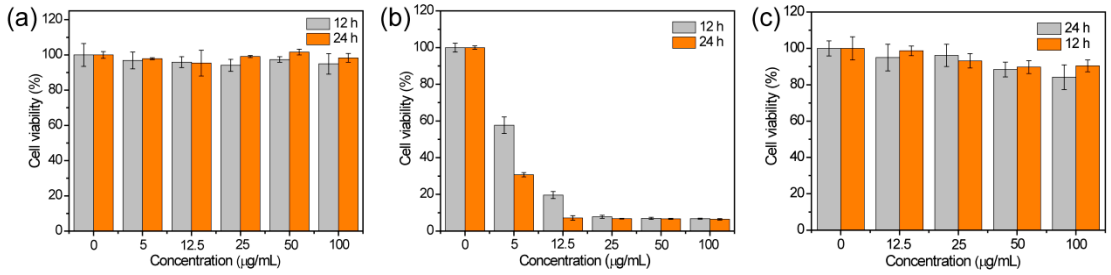

Figure 4. MTT assay of 4T1 cell viability after incubation of (**a**) Fe_3O_4-PAA, (**b**) Fe_3O_4-PAH and (**c**) Fe_3O_4-PVA at different concentrations of Fe for 12 and 24 h.

3.4. In Vivo Magnetic Resonance Imaging

The T_1-weight images with 4T1 tumor-bearing mice as the model were studied on a 1 T MRI scanner. Before intravenous injection of the materials, T_1-weight images of the coronal planes as control groups were acquired on the MRI scanner, and then the mice were intravenously injected with Fe_3O_4-PAA/Fe_3O_4-PVA with a dose of 1.3 mg Fe/kg body weight, and acquired the T_1-weight at different time points. As shown in Figure 5a, compared with the control group, the mice tumor and kidney sites brightened after 30 min, and gradually brightened with increasing time, suggesting Fe_3O_4-PAA displayed T_1-weight contrast enhancement in these sites. To quantify the contrast, the signal-to-noise ratio was calculated through analyzing the target sites and the normal tissues of the T_1-weight image. As shown in Figure 5b,c, after intravenous injection of Fe_3O_4-PAA, the relative signal-to-noise ratio of the tumor site reached the maximum (increased to about 65%) at 160 min, and that of the kidney site reached the maximum (increased to about 49%) at 60 min and remained almost unchanged for about 100 min. The increased T_1 signals at the tumor and kidney sites can be attributed to the accumulation of Fe_3O_4-PAA nanoparticles that instinctively featured T_1 contrast enhancement at these sites. After 180 min, the relative signal-to-noise ratio of both the tumor and kidney sites decreased slowly, indicating the metabolism of the nanoparticles. These results demonstrated that Fe_3O_4-PAA should be a good T_1-weight contrast agent for in vivo MR imaging.

Similar to Fe_3O_4-PAA, the T_1-weight images of 4T1 tumor-bearing mice slightly brightened the contrast enhancement at the tumor and kidney sites after intravenous injection of Fe_3O_4-PVA for 40 min (Figure 6a). The T_1-weight signal reached the increased maximum of about 53% at 120 min for the tumor site (Figure 6b), and 17% at 120 min for the kidney site (Figure 6c), indicating that the Fe_3O_4-PVA were slowly accumulated and displayed T_1 contrast enhancement in these sites. After 180 min, the relative signal-to-noise ratio of both tumor and kidney sites decreased slowly, suggesting the slow metabolism of the Fe_3O_4-PVA nanoparticles. The brightened contrast of the mice tumor and kidney sites demonstrated that Fe_3O_4-PVA can also be used as T_1-weight MRI contrast agent. Nevertheless, the increased T_1-weight signals at the tumor and kidney sites after intravenous injection of Fe_3O_4-PVA were slightly weaker than that for Fe_3O_4-PAA, indicating that Fe_3O_4-PAA would be a better T_1-weight contrast agent.

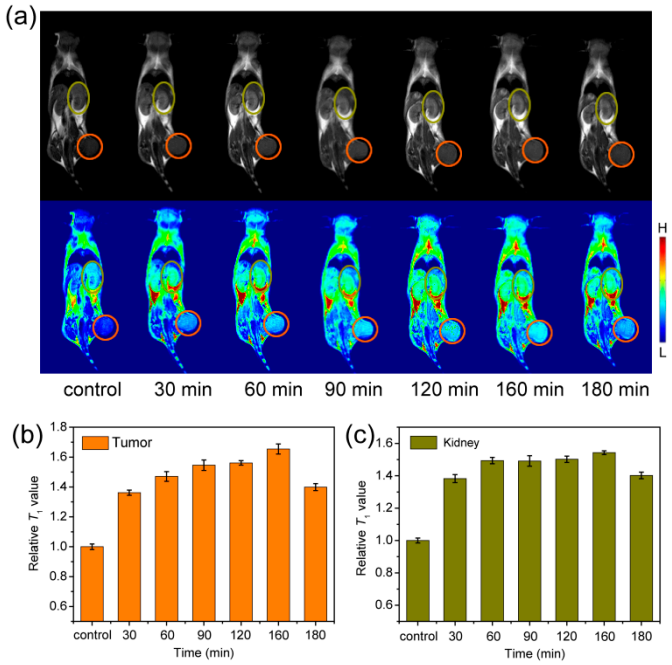

Figure 5. (**a**) T_1-weighted MR images (B_0 = 1 T) of mice collected before (control group) and after intravenous injection of Fe_3O_4-PAA at time points of 30, 60, 90, 120, 160 and 180 min. The corresponding relative T_1-weighted signals extracted from (**b**) tumor (orange circle) and (**c**) kidney (dark yellow circle) sites.

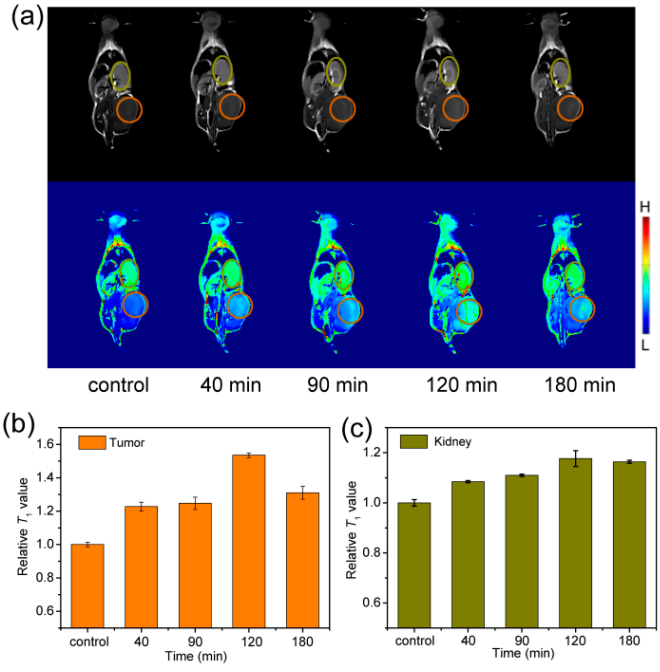

Figure 6. (**a**) T_1-weighted MR images (B_0 = 1 T) of mice collected before (control group) and after intravenous injection of Fe_3O_4-PVA at time points of 40, 90, 120 and 180 min. The corresponding relative T_1-weighted signals extracted from (**b**) tumor (orange circle) and (**c**) kidney (dark yellow circle) sites.

4. Conclusions

In summary, Fe_3O_4 nanoparticles with the surface modified by negative, positive and neutral macromolecule ligands of PAA, PAH and PVA, respectively, were synthesized using the coprecipitation

reaction. The obtained Fe_3O_4-PAA, Fe_3O_4-PAH, and Fe_3O_4-PVA nanoparticles showed slight differences in size and water-dispersibility. Besides, Fe_3O_4 nanoparticles modified with PAA and PVA showed good biocompatibility, while those modified using PAH displayed high cytotoxicity during cell viability assay. In vitro and in vivo experiments demonstrated that both Fe_3O_4-PAA and Fe_3O_4-PVA are adequate as T_1-weighted contrast agents, but Fe_3O_4-PAA exhibited a better T_1 contrast performance. This work highlights that the macromolecule ligands for modifying the Fe_3O_4 nanoparticles greatly affect their biocompatibility and T_1 contrast performance, which should be helpful for the design of functional ligands for developing Fe_3O_4 based T_1 contrast agents.

Supplementary Materials: The following are available online at http://www.mdpi.com/2079-4991/9/5/699/s1, Figure S1: Particle size distribution of (a) Fe_3O_4-PAA, (b) Fe_3O_4-PAH and (c) Fe_3O_4-PVA acquired from the TEM images. Figure S2: The hydrodynamic size profile of (a) Fe_3O_4-PAA, (b) Fe_3O_4-PAH and (c) Fe_3O_4-PVA nanoparticles in aqueous suspension.

Author Contributions: J.L. and S.Y. conceived and designed the experiments. C.T., Y.C. (Yanan Chen), D.W., Y.C. (Yu Cai) and Q.Z. carried out the experiments and drafted the manuscript. L.A., Q.T. and J.L. performed the analysis. All authors discussed and approved the final manuscript.

Funding: This research was funded by National Natural Science Foundation of China (Nos. 21601124, 21671135 and 21701111), Shanghai Sailing Program (17YF1413700), Ministry of Education of China (PCSIRT_IRT_16R49), and International Joint Laboratory on Resource Chemistry (IJLRC).

Conflicts of Interest: The authors declare no conflict of interest.

References

1. Lee, N.; Yoo, D.; Ling, D.; Cho, M.H.; Hyeon, T.; Cheon, J. Iron oxide based nanoparticles for multimodal imaging and magnetoresponsive therapy. *Chem. Rev.* **2015**, *115*, 10637–10689. [CrossRef] [PubMed]
2. Shen, Z.; Wu, A.; Chen, X. Iron oxide nanoparticle based contrast agents for magnetic resonance imaging. *Mol. Pharm.* **2017**, *14*, 1352–1364. [CrossRef] [PubMed]
3. Hu, Y.; Mignani, S.; Majoral, J.-P.; Shen, M.; Shi, X. Construction of iron oxide nanoparticle-based hybrid platforms for tumor imaging and therapy. *Chem. Soc. Rev.* **2018**, *47*, 1874–1900. [CrossRef]
4. Zhou, Z.; Wang, L.; Chi, X.; Bao, J.; Yang, L.; Zhao, W.; Chen, Z.; Wang, X.; Chen, X.; Gao, J. Engineered iron-oxide-based nanoparticles as enhanced T_1 contrast agents for efficient tumor imaging. *ACS Nano* **2013**, *7*, 3287–3296. [CrossRef]
5. Fernández-Barahona, I.; Gutiérrez, L.; Veintemillas-Verdaguer, S.; Pellico, J.; Morales, M.d.P.; Catala, M.; del Pozo, M.A.; Ruiz-Cabello, J.; Herranz, F. Cu-doped extremely small iron oxide nanoparticles with large longitudinal relaxivity: One-pot synthesis and in vivo targeted molecular imaging. *ACS Omega* **2019**, *4*, 2719–2727.
6. Pellico, J.; Ruiz-Cabello, J.; Fernández-Barahona, I.; Gutiérrez, L.; Lechuga-Vieco, A.V.; Enríquez, J.A.; Morales, M.P.; Herranz, F. One-step fast synthesis of nanoparticles for MRI: Coating chemistry as the key variable determining positive or negative contrast. *Langmuir* **2017**, *33*, 10239–10247. [CrossRef] [PubMed]
7. Liu, G.; Gao, J.; Ai, H.; Chen, X. Applications and potential toxicity of magnetic iron oxide nanoparticles. *Small* **2013**, *9*, 1533–1545. [CrossRef] [PubMed]
8. Wahsner, J.; Gale, E.M.; Rodríguez-Rodríguez, A.; Caravan, P. Chemistry of MRI contrast agents: Current challenges and new frontiers. *Chem. Rev.* **2019**. [CrossRef] [PubMed]
9. Caravan, P. Strategies for increasing the sensitivity of gadolinium based MRI contrast agents. *Chem. Soc. Rev.* **2006**, *35*, 512–523. [CrossRef] [PubMed]
10. Levy, M.; Luciani, N.; Alloyeau, D.; Elgrabli, D.; Deveaux, V.; Pechoux, C.; Chat, S.; Wang, G.; Vats, N.; Gendron, F.; et al. Long term in vivo biotransformation of iron oxide nanoparticles. *Biomaterials* **2011**, *32*, 3988–3999. [CrossRef] [PubMed]
11. Arami, H.; Khandhar, A.; Liggitt, D.; Krishnan, K.M. In vivo delivery, pharmacokinetics, biodistribution and toxicity of iron oxide nanoparticles. *Chem. Soc. Rev.* **2015**, *44*, 8576–8607. [CrossRef] [PubMed]
12. Mahmoudi, M.; Hofmann, H.; Rothen-Rutishauser, B.; Petri-Fink, A. Assessing the in vitro and in vivo toxicity of superparamagnetic iron oxide nanoparticles. *Chem. Rev.* **2012**, *112*, 2323–2338. [CrossRef]

13. Penfield, J.G.; Reilly, R.F., Jr. What nephrologists need to know about gadolinium. *Nat. Clin. Pract. Nephrol.* **2007**, *3*, 654. [CrossRef]
14. Tromsdorf, U.I.; Bruns, O.T.; Salmen, S.C.; Beisiegel, U.; Weller, H. A highly effective, nontoxic T_1 MR contrast agent based on ultrasmall PEGylated iron oxide nanoparticles. *Nano Lett.* **2009**, *9*, 4434–4440. [CrossRef] [PubMed]
15. Kim, B.H.; Lee, N.; Kim, H.; An, K.; Park, Y.I.; Choi, Y.; Shin, K.; Lee, Y.; Kwon, S.G.; Na, H.B.; et al. Large-scale synthesis of uniform and extremely small-sized iron oxide nanoparticles for high-resolution T_1 magnetic resonance imaging contrast agents. *J. Am. Chem. Soc.* **2011**, *133*, 12624–12631. [CrossRef]
16. Shen, Z.; Song, J.; Zhou, Z.; Yung, B.C.; Aronova, M.A.; Li, Y.; Dai, Y.; Fan, W.; Liu, Y.; Ruan, H.; et al. Dotted core–shell nanoparticles for T_1-weighted MRI of tumors. *Adv. Mater.* **2018**, *30*, 1803163. [CrossRef]
17. Borase, T.; Ninjbadgar, T.; Kapetanakis, A.; Roche, S.; O'Connor, R.; Kerskens, C.; Heise, A.; Brougham, D.F. Stable aqueous dispersions of glycopeptide-grafted selectably functionalized magnetic nanoparticles. *Angew. Chem. Int. Ed.* **2013**, *52*, 3164–3167. [CrossRef] [PubMed]
18. Hannecart, A.; Stanicki, D.; Vander Elst, L.; Muller, R.N.; Lecommandoux, S.; Thévenot, J.; Bonduelle, C.; Trotier, A.; Massot, P.; Miraux, S.; et al. Nano-thermometers with thermo-sensitive polymer grafted USPIOs behaving as positive contrast agents in low-field MRI. *Nanoscale* **2015**, *7*, 3754–3767. [CrossRef]
19. Wang, L.; Huang, J.; Chen, H.; Wu, H.; Xu, Y.; Li, Y.; Yi, H.; Wang, Y.A.; Yang, L.; Mao, H. Exerting enhanced permeability and retention effect driven delivery by ultrafine iron oxide nanoparticles with T_1–T_2 switchable magnetic resonance imaging contrast. *ACS Nano* **2017**, *11*, 4582–4592. [CrossRef] [PubMed]
20. Bai, C.; Jia, Z.; Song, L.; Zhang, W.; Chen, Y.; Zang, F.; Ma, M.; Gu, N.; Zhang, Y. Magnetic resonance imaging: Time-dependent T_1–T_2 switchable magnetic resonance imaging realized by c(RGDyK) modified ultrasmall Fe_3O_4 nanoprobes. *Adv. Funct. Mater.* **2018**, *28*, 1870221. [CrossRef]
21. Xie, J.; Liu, G.; Eden, H.S.; Ai, H.; Chen, X. Surface-engineered magnetic nanoparticle platforms for cancer imaging and therapy. *Acc. Chem. Res.* **2011**, *44*, 883–892. [CrossRef]
22. Zeng, J.; Jing, L.; Hou, Y.; Jiao, M.; Qiao, R.; Jia, Q.; Liu, C.; Fang, F.; Lei, H.; Gao, M. Anchoring group effects of surface ligands on magnetic properties of Fe_3O_4 nanoparticles: Towards high performance MRI contrast agents. *Adv. Mater.* **2014**, *26*, 2694–2698. [CrossRef]
23. Kang, T.; Li, F.; Baik, S.; Shao, W.; Ling, D.; Hyeon, T. Surface design of magnetic nanoparticles for stimuli-responsive cancer imaging and therapy. *Biomaterials* **2017**, *136*, 98–114. [CrossRef]
24. Sun, H.; Zhang, B.; Jiang, X.; Liu, H.; Deng, S.; Li, Z.; Shi, H. Radiolabeled ultra-small Fe_3O_4 nanoprobes for tumor-targeted multimodal imaging. *Nanomedicine* **2019**, *14*, 5–17. [CrossRef]
25. Nguyen, V.T.A.; Gauthier, M.; Sandre, O. Templated synthesis of magnetic nanoparticles through the self-assembly of polymers and surfactants. *Nanomaterials* **2014**, *4*, 628–685. [CrossRef]
26. Li, Z.; Yi, P.W.; Sun, Q.; Lei, H.; Li Zhao, H.; Zhu, Z.H.; Smith, S.C.; Lan, M.B.; Lu, G.Q. Ultrasmall water-soluble and biocompatible magnetic iron oxide nanoparticles as positive and negative dual contrast agents. *Adv. Funct. Mater.* **2012**, *22*, 2387–2393. [CrossRef]
27. Shen, Z.; Chen, T.; Ma, X.; Ren, W.; Zhou, Z.; Zhu, G.; Zhang, A.; Liu, Y.; Song, J.; Li, Z.; et al. Multifunctional theranostic nanoparticles based on exceedingly small magnetic iron oxide nanoparticles for T_1-weighted magnetic resonance imaging and chemotherapy. *ACS Nano* **2017**, *11*, 10992–11004. [CrossRef]
28. Qiao, R.; Yang, C.; Gao, M. Superparamagnetic iron oxide nanoparticles: From preparations to in vivo MRI applications. *J. Mater. Chem.* **2009**, *19*, 6274–6293. [CrossRef]
29. Maggioni, D.; Arosio, P.; Orsini, F.; Ferretti, A.M.; Orlando, T.; Manfredi, A.; Ranucci, E.; Ferruti, P.; D'Alfonso, G.; Lascialfari, A. Superparamagnetic iron oxide nanoparticles stabilized by a poly(amidoamine)-rhenium complex as potential theranostic probe. *Dalton Trans.* **2014**, *43*, 1172–1183. [CrossRef]
30. Zhu, Y.; Lei, J.; Tian, Y. Uniform iron oxide hollow spheres for high-performance delivery of insoluble anticancer drugs. *Dalton Trans.* **2014**, *43*, 7275–7281. [CrossRef]
31. Wu, L.; Mendoza-Garcia, A.; Li, Q.; Sun, S. Organic phase syntheses of magnetic nanoparticles and their applications. *Chem. Rev.* **2016**, *116*, 10473–10512. [CrossRef] [PubMed]
32. Sun, S.; Zeng, H.; Robinson, D.B.; Raoux, S.; Rice, P.M.; Wang, S.X.; Li, G. Monodisperse MFe_2O_4 (M = Fe, Co, Mn) Nanoparticles. *J. Am. Chem. Soc.* **2004**, *126*, 273–279. [CrossRef]

33. Cotin, G.; Kiefer, C.; Perton, F.; Ihiawakrim, D.; Blanco-Andujar, C.; Moldovan, S.; Lefevre, C.; Ersen, O.; Pichon, B.; Mertz, D.; et al. Unravelling the thermal decomposition parameters for the synthesis of anisotropic iron oxide nanoparticles. *Nanomaterials* **2018**, *8*, 881. [CrossRef]
34. Lu, A.-H.; Salabas, E.L.; Schüth, F. Magnetic nanoparticles: Synthesis, protection, functionalization, and application. *Angew. Chem. Int. Ed.* **2007**, *46*, 1222–1244. [CrossRef]
35. Li, J.; Hu, Y.; Yang, J.; Sun, W.; Cai, H.; Wei, P.; Sun, Y.; Zhang, G.; Shi, X.; Shen, M. Facile synthesis of folic acid-functionalized iron oxide nanoparticles with ultrahigh relaxivity for targeted tumor MR imaging. *J. Mater. Chem. B* **2015**, *3*, 5720–5730. [CrossRef]
36. Sun, W.; Yang, J.; Zhu, J.; Zhou, Y.; Li, J.; Zhu, X.; Shen, M.; Zhang, G.; Shi, X. Immobilization of iron oxide nanoparticles within alginate nanogels for enhanced MR imaging applications. *Biomater. Sci.* **2016**, *4*, 1422–1430. [CrossRef]
37. Shen, L.-H.; Bao, J.-F.; Wang, D.; Wang, Y.-X.; Chen, Z.-W.; Ren, L.; Zhou, X.; Ke, X.-B.; Chen, M.; Yang, A.-Q. One-step synthesis of monodisperse, water-soluble ultra-small Fe_3O_4 nanoparticles for potential bio-application. *Nanoscale* **2013**, *5*, 2133–2141. [CrossRef]
38. Hu, H.; Yang, H.; Huang, P.; Cui, D.; Peng, Y.; Zhang, J.; Lu, F.; Lian, J.; Shi, D. Unique role of ionic liquid in microwave-assisted synthesis of monodisperse magnetite nanoparticles. *Chem. Commun.* **2010**, *46*, 3866–3868. [CrossRef]
39. Rui, Y.-P.; Liang, B.; Hu, F.; Xu, J.; Peng, Y.-F.; Yin, P.-H.; Duan, Y.; Zhang, C.; Gu, H. Ultra-large-scale production of ultrasmall superparamagnetic iron oxide nanoparticles for T_1-weighted MRI. *RSC Adv.* **2016**, *6*, 22575–22585. [CrossRef]
40. Gupta, A.K.; Gupta, M. Synthesis and surface engineering of iron oxide nanoparticles for biomedical applications. *Biomaterials* **2005**, *26*, 3995–4021. [CrossRef] [PubMed]
41. Mintzer, M.A.; Grinstaff, M.W. Biomedical applications of dendrimers: A tutorial. *Chem. Soc. Rev.* **2011**, *40*, 173–190. [CrossRef] [PubMed]
42. Lam, T.; Avti, P.K.; Pouliot, P.; Maafi, F.; Tardif, J.-C.; Rhéaume, É.; Lesage, F.; Kakkar, A. Fabricating water dispersible superparamagnetic iron oxide nanoparticles for biomedical applications through ligand exchange and direct conjugation. *Nanomaterials* **2016**, *6*, 100. [CrossRef] [PubMed]
43. Amstad, E.; Textor, M.; Reimhult, E. Stabilization and functionalization of iron oxide nanoparticles for biomedical applications. *Nanoscale* **2011**, *3*, 2819–2843. [CrossRef]
44. Koczkur, K.M.; Mourdikoudis, S.; Polavarapu, L.; Skrabalak, S.E. Polyvinylpyrrolidone (PVP) in nanoparticle synthesis. *Dalton Trans.* **2015**, *44*, 17883–17905. [CrossRef] [PubMed]
45. Xiao, W.; Legros, P.; Chevallier, P.; Lagueux, J.; Oh, J.K.; Fortin, M.-A. Superparamagnetic iron oxide nanoparticles stabilized with multidentate block copolymers for optimal vascular contrast in T_1-weighted magnetic resonance imaging. *ACS Appl. Nano Mater.* **2018**, *1*, 894–907. [CrossRef]
46. Huang, J.; Wang, L.; Zhong, X.; Li, Y.; Yang, L.; Mao, H. Facile non-hydrothermal synthesis of oligosaccharide coated sub-5 nm magnetic iron oxide nanoparticles with dual MRI contrast enhancement effects. *J. Mater. Chem. B* **2014**, *2*, 5344–5351. [CrossRef]
47. Calatayud, M.P.; Sanz, B.; Raffa, V.; Riggio, C.; Ibarra, M.R.; Goya, G.F. The effect of surface charge of functionalized Fe_3O_4 nanoparticles on protein adsorption and cell uptake. *Biomaterials* **2014**, *35*, 6389–6399. [CrossRef]
48. Asati, A.; Santra, S.; Kaittanis, C.; Perez, J.M. Surface-charge-dependent cell localization and cytotoxicity of cerium oxide nanoparticles. *ACS Nano* **2010**, *4*, 5321–5331. [CrossRef]
49. Ahn, T.; Kim, J.H.; Yang, H.-M.; Lee, J.W.; Kim, J.-D. Formation pathways of magnetite nanoparticles by coprecipitation method. *J. Phys. Chem. C* **2012**, *116*, 6069–6076. [CrossRef]
50. Nasrollahi, F.; Varshosaz, J.; Khodadadi, A.A.; Lim, S.; Jahanian-Najafabadi, A. Targeted delivery of docetaxel by use of transferrin/poly(allylamine hydrochloride)-functionalized graphene oxide nanocarrier. *ACS Appl. Mater. Interf.* **2016**, *8*, 13282–13293. [CrossRef]
51. Du, W.; Jiang, L.; Shi, M.; Yang, Z.; Zhang, X. The modification mechanism and the effect of magnesium chloride on poly(vinyl alcohol) films. *RSC Adv.* **2019**, *9*, 1602–1612. [CrossRef]
52. Demortière, A.; Panissod, P.; Pichon, B.P.; Pourroy, G.; Guillon, D.; Donnio, B.; Bégin-Colin, S. Size-dependent properties of magnetic iron oxide nanocrystals. *Nanoscale* **2011**, *3*, 225–232. [CrossRef] [PubMed]

53. Li, D.; Hua, M.; Fang, K.; Liang, R. BSA directed-synthesis of biocompatible Fe_3O_4 nanoparticles for dual-modal T_1 and T_2 MR imaging in vivo. *Anal. Methods* **2017**, *9*, 3099–3104. [CrossRef]
54. Safi, M.; Sarrouj, H.; Sandre, O.; Mignet, N.; Berret, J.F. Interactions between sub-10-nm iron and cerium oxide nanoparticles and 3T3 fibroblasts: The role of the coating and aggregation state. *Nanotechnology* **2010**, *21*, 145103. [CrossRef] [PubMed]